

Thermal relaxation of molecular oxygen in collisions with nitrogen atoms

Daniil A. Andrienko^{a)} and Iain D. Boyd

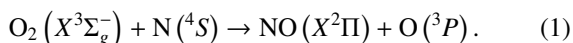
Department of Aerospace Engineering, University of Michigan, 1320 Beal Ave., Ann Arbor, Michigan 48108, USA

(Received 10 February 2016; accepted 21 June 2016; published online 6 July 2016)

Investigation of O₂–N collisions is performed by means of the quasi-classical trajectory method on the two lowest *ab initio* potential energy surfaces at temperatures relevant to hypersonic flows. A complete set of bound–bound and bound–free transition rates is obtained for each precollisional rovibrational state. Special attention is paid to the vibrational and rotational relaxations of oxygen as a result of chemically non-reactive interaction with nitrogen atoms. The vibrational relaxation of oxygen partially occurs via the formation of an intermediate NO₂ complex. The efficient energy randomization results in rapid vibrational relaxation at low temperatures, compared to other molecular systems with a purely repulsive potential. The vibrational relaxation time, computed by means of master equation studies, is nearly an order of magnitude lower than the relaxation time in N₂–O collisions. The rotational nonequilibrium starts to play a significant effect at translational temperatures above 8000 K. The present work provides convenient relations for the vibrational and rotational relaxation times as well as for the quasi-steady dissociation rate coefficient and thus fills a gap in data due to a lack of experimental measurements for this system. *Published by AIP Publishing*. [<http://dx.doi.org/10.1063/1.4955199>]

I. INTRODUCTION

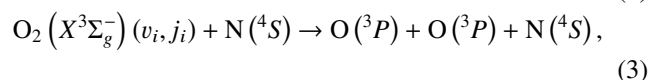
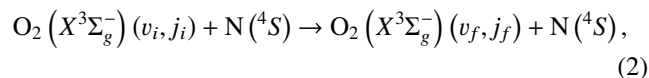
The interaction of oxygen molecules with nitrogen atoms is important in shock heated air, the chemistry of the upper atmosphere, and the combustion of carbon-based fuels. The formation of nitric oxide in these applications occurs via the Zeldovich mechanism,¹



It is well known that the product of reaction (1) has a strong non-Boltzmann distribution of vibrational quanta.^{2–4} The rate of reaction (1) as well as the process of NO quenching by molecular oxygen sets a background for the explanation of infrared chemiluminescence in the upper atmosphere. A considerable amount of work,^{5,6} besides that already mentioned, has been devoted to the study of the Zeldovich mechanism.

However, the O₂–N nonreactive channel of the interaction can also be important in modeling flows with a large number of nitrogen atoms. State-specific data on O₂–N collisions become necessary when attempting to develop high fidelity thermochemistry models of nonequilibrium hypersonic flows. During the past decade, a significant amount of work dealing with the state-resolved chemistry of nitrogen has been conducted.^{4,7–10} The chemistry of molecular oxygen is studied less often, mainly due to the relatively rapid O₂ dissociation in hypersonic flows, generated during the reentry of spacecraft. However, a significant amount of oxygen is encountered during the flight of hypersonic vehicles at moderate velocity. Meanwhile, to the authors' knowledge, a model of oxygen relaxation in collisions with nitrogen atoms has not been proposed yet. Taking these facts into account, it is of interest

to revisit the following reactions:



using the most recent theoretical data. The experimental study of the O₂–N system is complicated due to the large difference in dissociation energies of oxygen and nitrogen molecules. The presence of fast chemical reactions involving nitric oxide also complicates measurements of the vibrational distribution of products. As a result, experimental data on oxygen relaxation in O₂–N collisions are absent. To overcome this difficulty, an equality of relaxation times in O₂–N and N₂–O collisions has been assumed in computational models of hypersonic flows.¹¹ While this assumption can be partially justified due to the similar masses of reactants, state-to-state reaction rates are desirable for the implementation of more accurate state-resolved models of hypersonic flows.

The present work adopts two recently generated ²A' and ⁴A' potential energy surfaces (PESs) based on the *ab initio* calculations of a large number of points in the C_s and C_{2v} configurations¹² of the NO₂ molecular system. These new PESs provide accurate curve fitted relations for over 1500 and 900 *ab initio* points, respectively, and more realistic values of the potential barrier compared to previously reported data.⁵

This paper is organized as follows: Section II describes the basic properties of the potential energy surfaces and addresses the governing equations of the quasi-classical trajectory (QCT) method and kinetic equations. Section III consists of multiple subsections and discusses the results of the present study. Subsection III A compares the present thermal relaxation rates with those previously reported in the literature. Subsection

^{a)}Electronic mail: daniila@umich.edu.

III B discusses the specifics of vibrational and rotational relaxations. Subsection III D presents a comparison of the master equation approach with the multi-temperature model. Subsection III C presents the results on coupling of thermal relaxation with the depletion mechanism of oxygen in a bath of nitrogen atoms. Conclusions are drawn in Section IV.

II. METHODOLOGY

A. Molecular structure and potential energy surfaces

The Zeldovich mechanism proceeds via the two lowest $^2A'$ and $^4A'$ potential energy surfaces. The experimentally measured potential barriers of these PESs are 0.355 and 0.694 eV, respectively. At temperatures below 5000 K, collisions of molecular oxygen with atomic nitrogen proceed mostly on the ground $^2A'$ PES, while at higher temperatures, observed in hypersonic flows, it is important to account for both of the $^2A'$ and $^4A'$ PES contributions. The O_2 –N collisions that induce the bound–bound transition of oxygen (nonreactive channel) also occur on the excited $^6A'$ potential energy surface. However, it is expected that the contribution of this PES is small in the range of temperatures from 1000 to 15 000 K, due to the relatively high potential energy barrier. The $^6A'$ PES correlates with the first excited electronic state $NO(a^4\Pi)$ with an energy of 4.8 eV above the ground configuration. Because an analytical form of the $^6A'$ PES is not yet proposed in the literature, the investigation of O_2 –N collisions is possible only by taking into account the $^2A'$ and $^4A'$ PESs in the range of low to moderate temperatures. In the present work, thermal relaxation of O_2 is considered only on $^2A'$ and $^4A'$ PESs. Simulations of simultaneous kinetic processes on these PES include appropriate statistical weights. Namely, the rate coefficients of bound–bound transitions between internal states of oxygen are calculated using the following relation:

$$K(^6A') = \frac{1}{6} K(^2A') + \frac{1}{3} K(^4A'). \quad (4)$$

However, the dissociation process can occur on $^6A'$ PES as well. This process contributes with the statistical weight of 1/2. It will be shown later that dissociation rate coefficients for $^2A'$ and $^4A'$ PESs have close values, and the contribution of $^6A'$ PES presumably doubles the total dissociation rate coefficient. Following this approximation, it is possible to include the contribution of $^6A'$ PES. Nevertheless, detailed QCT simulations are required in future when $^6A'$ PES becomes available. At high temperatures $^6A'$ PES may contribute to exchange and inelastic processes as well. However, due to unavailability of such PES, these types of reactions are considered only on $^2A'$ and $^4A'$ PESs. For consistency, the investigation of thermal relaxation is performed simultaneously on $^2A'$ and $^4A'$ PESs with the dissociation rate coefficients computed only accounting for two lowest PESs with appropriate multiplicities. However the tabulated global dissociation rate coefficients are derived using the following relation:

$$D = 2 \left[\frac{1}{6} D(^2A') + \frac{1}{3} D(^4A') \right]. \quad (5)$$

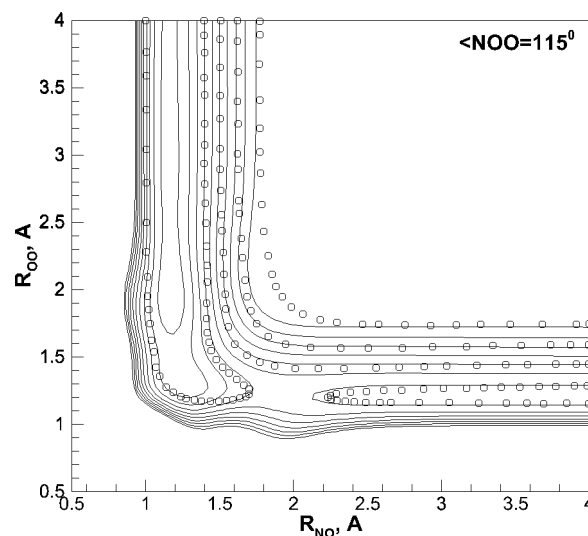


FIG. 1. $^2A'$ O_2N PESs, solid lines—Sayós *et al.*,¹² symbols - curve fit of Ref. 5 by Bose and Candler.⁴

The equipotential curves between -2 and -6.5 eV with the step of 0.5 eV of the $^2A'$ and $^4A'$ surfaces by Sayós *et al.*¹² are shown in Figs. 1 and 2 by solid lines, respectively. The angles between the O–O and N–O bonds are set to 115° and 109.4° in order to perform direct comparison with PESs by Bose and Candler.⁴ In the latter, the *ab initio* data by Walch and Jaffe^{5,13} were used to construct PES. Note that the $^2A'$ PES correlates with $NO_2(X^2A_1)$. The $^2A'$ and $^4A'$ PESs have potential barriers of 0.299 and 0.557 eV, respectively, which appears to be the closest agreement to the experimental data. For reference, the equipotential levels between -2 and -5 eV of $^2A'$ and $^4A'$ PESs generated by Bose and Candler⁴ are shown in Figs. 1 and 2 by symbols. One can see some apparent differences between these two sets of potential energy surfaces. The potential well at small intermolecular distances is less steep in PES by Sayós. The location of the saddle point in Bose and Candler and Sayós calculations agrees better for

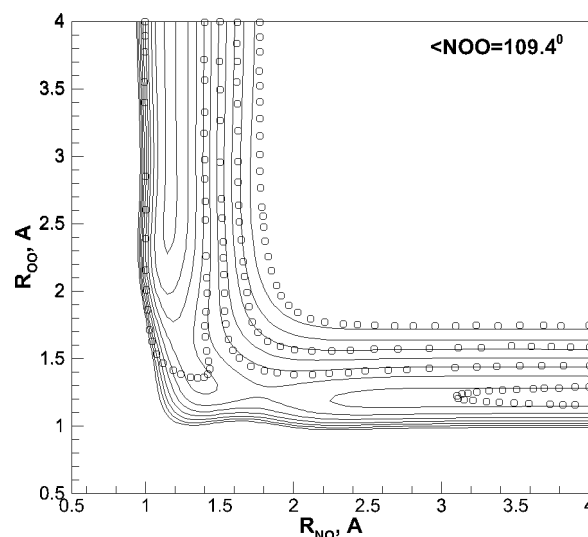


FIG. 2. $^4A'$ O_2N PESs, solid lines—Sayós *et al.*,¹² symbols - curve fit of Ref. 5 by Bose and Candler.⁴

$2A'$ PESs, compared to the $4A'$ PES. It will be shown later that these observations lead to some differences in state-specific cross sections and thermal rates.

Some words should be said about the molecular structure of the ground electronic state of oxygen molecule. The symmetry of this state is $3\Sigma_g^-$, which means that the second Hund's case is applicable to the electron angular momentum and spin, respectively, $\Lambda = 0$ and $S = 1$. The corresponding quantum number of the total angular momentum apart from spin (K) is identical to the quantum number of the rotational motion of nuclei (N), and thus takes all positive integer values, starting from 0. The total angular momentum, J , takes non-negative values according to the principles of vector addition,

$$J = N + S, N + S - 1, N + S - 2, \dots, |N - S|. \quad (6)$$

Thus, each rotational level (except $K = 0$) is slightly split into three components according to the spin multiplicity. This is due to the small magnetic field induced by the rotation of molecule which results in the spin-rotation ($K - S$) coupling. This splitting is an order of several $1/\text{cm}$,¹⁴ which is clearly much less than the accuracy of PESs, as discussed above. Each rotational level is presented by the triplet structure with the same N and three possible values of J . The rules of nuclear spin statistics dictate the absence of states with even N .¹⁵ The rigorous implementation of selection rules would involve the restriction of ΔJ to be even by allowing J to take all integer values and N to take only odd values. This corresponds to the strong favoring of states with the same e/f parity.¹⁵ Following this approach, the states with even $J = N + 1, N - 1$ have weight of $2/3$ and states with odd $J = N$ have weight of $1/3$. However, taking into account small value of splitting with respect to hypersonic energies, the present work adopts a simpler treatment of nuclear spin statistics. All transitions are restricted to even ΔJ and states with $J = N$ are assigned a statistical weight of 1 if N is odd and 0 if N is even, while transitions from $J = N + 1$ and $J = N - 1$ are not considered. This approach allows for a significant reduction of computational cost of the state-specific model while retaining all major properties of oxygen kinetics.

B. QCT method

In the present work, the Quasi-Classical Trajectory (QCT) method is used to generate vibrationally resolved transition cross sections of reactions (1)-(3). The initial rovibrational state, (v_i, j_i) , is fixed in each batch of trajectories. The internuclear separation in the isolated oxygen molecule is initialized by the random sampling of oscillation phase based on the period of vibrational motion. Initial separation of the target and projectile particles is given by 15 Å. Hamilton's differential equations, described in Ref. 16, are solved by the Adams-Moulton method of 11th order of accuracy. The impact parameter, b , is sampled randomly from each strata with the size of 0.1 Å. Every batch contains 2×10^3 trajectories. Analysis of the final state is performed according to Ref. 16. Each trajectory is integrated with an error in the total energy not exceeding $10^{-4}\%$. A trajectory is terminated after the distance between products exceeds the

initial separation. Each such trajectory is then classified into one of the three possible channels: non-reactive bound-bound transition, exchange reaction, or dissociation (bound-free transition). The probability, Φ , of the state-specific transition $(v_i, j_i) \rightarrow (v_f, j_f)$, where (v_f, j_f) is the final rovibrational state, at a given collision energy E_{col} , is defined as follows:

$$\Phi(E_{col}) = \frac{2}{b_{max}^2} \int_0^{b_{max}} \left(\frac{N_{v_i j_i \rightarrow v_f j_f}}{N} \right) b db, \quad (7)$$

where b_{max} is the impact parameter at which only elastic collisions are observed, $N_{v_i j_i \rightarrow v_f j_f}$ and N are the number of trajectories with the desired transition and the total number of trajectories in the current batch of impact parameter, respectively. The probability of the bound-free transition is calculated in a manner similar to Eq. (7). The cross section of either bound-bound or bound-free transition is calculated as follows:

$$\sigma(E_{col}, v_i, j_i) = \pi b_{max}^2 \Phi(E_{col}, v_i, j_i), \quad (8)$$

where Φ is sampled over the five variables besides those mentioned in Eq. (8): impact parameter, initial azimuthal and polar orientations of the target molecule, initial orientation of the target molecule angular momentum, and initial vibrational phase of the target molecule. The reaction probability is also defined by the final rovibrational state as well as by the channel of interest. The present calculations study dynamics of O_2 -N collisions in the range of collision energy from 0.01 to 8 eV. This range is covered by 35 intervals of uneven length. Stratified sampling of the impact parameter is adopted to increase accuracy of statistical modeling. The procedure of trajectory simulation is repeated individually on the $2A'$ and $4A'$ PESs. The overall number of trajectories included in statistics is approximately 1.2×10^{10} for each surface.

The present study features the analysis of rates assuming trans-rotational equilibrium, as well as treating vibrational and rotational modes in a similar manner. As a first step in the analysis of the reaction rate dataset, trans-rotational equilibrium is assumed. In order to do so, the cross section of transition from the initial state to any final rotational state of the final vibrational level is computed as follows:

$$\sigma(E_{col}, v_i, j_i \rightarrow v_f) = \sum_{j_f} \sigma(E_{col}, v_i, j_i \rightarrow v_f, j_f). \quad (9)$$

The rate of either bound-bound or bound-free transition at the gas temperature T is calculated by integrating the corresponding cross sections,

$$K(v_i, j_i, T) = \frac{8\pi}{\sqrt{\mu_{N, O_2}}} (2\pi k_B T)^{-3/2} \times \int_0^\infty \sigma(E_{col}, v_i, j_i) E_{col} \exp\left(\frac{-E_{col}}{k_B T}\right) dE_{col}. \quad (10)$$

For further analysis, it is convenient to average the reaction rate over all rotational levels that belong to the initial vibrational state. The averaging procedure assumes that each rotational level j_i contributes to the rate according to the

Boltzmann factor w ,

$$w_{ji} = \epsilon g_e (2j_i + 1) \exp(-(e_{v_i,j_i} - e_{v_i,0})/k_B T), \quad (11)$$

where ϵ is the symmetry factor of O_2 , and g_e is the degeneracy of the electronic state. The Boltzmann-averaged rates of the bound-bound ($v_i \rightarrow v_f$) and bound-free ($v_i \rightarrow c$) transitions are derived using the following:

$$K_{v_i \rightarrow v_f} = \frac{\sum_{j_i} (w_{ji} \sum_{j_f} K_{v_i,j_i \rightarrow v_f,j_f})}{\sum_{j_i} w_{ji}}, \quad (12)$$

$$K_{v_i \rightarrow c} = \frac{\sum_{j_i} w_{ji} K_{v_i,j_i \rightarrow c}}{\sum_{j_i} w_{ji}}. \quad (13)$$

$$\begin{aligned} \frac{dn_i}{dt} = & \sum_{f \neq i} (K(T, v_i, j_i \rightarrow v_f, j_f) n_N n_f - K(T, v_f, j_f \rightarrow v_i, j_i) n_N n_i) \\ & + R(T, v_i, j_i) n_N n_O^2 - D(T, v_i, j_i) n_N n_i - T^f(v_i, j_i) n_i + T^b(v_i, j_i) n_O^2, \quad i = 1 \dots N_s, \quad f = 1 \dots N_s, \end{aligned} \quad (14)$$

where N_s is the total number of rovibrational states, and T^f and T^b are the forward and backward tunneling rate coefficients. The rates of bound-bound transitions are given by Eq. (10). Equation (14) describes the trans-rotational-vibrational energy transfer and is termed as the rotational-vibrational-translational (RVT) thermodynamic model. An implicit method of third order accuracy for diagonal and second order accuracy for off-diagonal elements is applied to integrate Eq. (14). The initial number density, given by $n_{O_2,0} + n_{N,0}$, is set to $1 \times 10^{18} \text{ cm}^{-3}$. This is equivalent to a pressure of 1.3626 atm at a gas temperature of 10 000 K. No mass exchange with the surrounding medium is allowed. To simulate conditions when the atom-molecule collisions are dominant, the initial number density of atomic oxygen is set to $\alpha = 0.99$ of the total number density, unless stated otherwise. At initial nonequilibrium conditions, the population of rovibrational states is given by the Boltzmann distribution with the temperature $T_0 = 100 \text{ K}$, as follows:

$$n_{i,0} = \frac{Q_i(T_{rot}, T_{vib})}{\sum_i Q_i(T_{rot}, T_{vib})} n_{O_2,0}, \quad (15)$$

where

$$\begin{aligned} Q_i(T_{rot}, T_{vib}) = & g_{j_i}^{NS} (2j_i + 1) \\ & \times \exp(-(e_{v_i,j_i} - e_{v_i,0})/k_B T_{rot}) \\ & \times \exp(-e_{v_i,0}/k_B T_{vib}) \end{aligned} \quad (16)$$

is the two-temperature rovibrational partition function, $g_{j_i}^{NS}$ is the O_2 nuclear spin degeneracy, and $n_{O_2,0}$ is the total number density of oxygen. The initial internal temperatures, $T_{rot,0}$ and $T_{vib,0}$, are equal to T_0 when the RVT model is applied.

The rate coefficients of endothermic processes are computed using the principle of detailed balance. The

C. System of master equations

The rates of rovibrational transitions are incorporated into the system of master equations in order to describe thermalization of internal degrees of freedom toward the equilibrium state. The present approach considers thermal relaxation for each rovibrational state as well as assuming the presence of rotational equilibrium. For the latter, the system of master equations is formulated for each vibrational state. The state-specific dissociation and recombination are included in the present formulation unless the opposite is stated. The quasi-bound (QB) states are assumed to have a finite lifetime unless the opposite is stated. Solution of master equations is obtained for translational temperatures between 500 and 20 000 K. The resulting system of equations for the number density of rovibrational level i can be written as follows:

following relation is used to compute the rate coefficient of the reverse bound-bound transition:

$$K(T, v_f, j_f \rightarrow v_i, j_i) = K(T, v_i, j_i \rightarrow v_f, j_f) \times \exp(-(e_{v_i,j_i} - e_{v_f,j_f})/k_B T), \quad (17)$$

where $e_{v_i,j_i} > e_{v_f,j_f}$. The recombination rate coefficient is estimated from the state-specific dissociation RC in the following way:

$$R(T, v_i, j_i) = D(T, v_i, j_i) \frac{Q_i Q_{t,i}}{Q_O^2 Q_{t,O}^2} \exp(D_{e,v_i,j_i}/k_B T), \quad (18)$$

where $Q_{t,i}$ is the translational partition function of state (v_i, j_i) , Q_O and $Q_{t,O}$ are the atomic and translational partition function of atomic oxygen, and D_{e,v_i,j_i} is the dissociation energy of i state. The rate coefficient of tunneling from bound state is calculated according to Ref. 17. The reverse rate coefficient is computed using Eq. (18).

The system of governing equations in the case of trans-rotational equilibrium has the following appearance:

$$\begin{aligned} \frac{dn_i}{dt} = & \sum_{f \neq i} (K(T, v_f \rightarrow v_i) n_N n_f - K(T, v_i \rightarrow v_f) n_N n_i) \\ & + R(T, v_f) n_N n_O^2 - D(T, v_i) n_N n_i - T^f(v_i) n_i \\ & + T^b(v_i) n_O^2, \quad i = 1 \dots N_v, \quad f = 1 \dots N_v, \end{aligned} \quad (19)$$

where N_v is the total number of vibrational states, D and R are the dissociation and recombination rate coefficients. Equation (19) describes the trans-vibrational energy transfer and is termed as the VT model. The initial rotational temperature is set to the heat bath temperature, and the initial vibrational temperature is set to T_0 .

The master equation approach does not imply the existence of internal temperature that governs the population

of rovibrational states. However, for post-processing analysis, the vibrational and rotational temperatures can be useful for describing the general properties of rovibrational manifold. In the present work, the energy-equivalent definition of internal temperature is adopted. Details of this approach are given in Ref. 18.

III. RESULTS

A. Study of NO formation

The variation of the cross section of reaction (1) with the energy of collision, is shown in Fig. 3 for initial state O_2 ($v_i = 0, j_i = 7$) and ($v_i = 0, j_i = 9$). The present data are compared to the results by Bose and Candler and by Gilibert *et al.*,¹⁹ given for the rovibrational state O_2 ($v_i = 0, j_i = 8$). It is impossible to perform a direct comparison since in the original works all rotational states of molecular oxygen were taken into account, while the quantum-mechanical rules of nuclear spin statistics¹⁴ dictate the absence of the even-numbered rotational states of oxygen due to zero nuclear spin.

In Fig. 3, the square symbols and solid line correspond to the present results obtained on the $^2A'$ PES for $j_i = 7$ and 9, respectively. The red dashed and blue dashed-dotted lines correspond to the data by Bose⁴ and Gilibert,¹⁹ respectively. The present calculations confirm the lower potential energy barrier of $^2A'$ PES,¹² compared to previously reported data. The difference in the cross sections increases at high collision energies. This can be explained by some disagreements in the PESs, shown in Figs. 1 and 2, in the region of small internuclear distances, inaccessible at small collision energies. At higher collision energies, the present results are in agreement with the work by Gilibert *et al.* which used the same *ab initio* data by Jaffe *et al.*⁵ with a different curve fit technique. As discussed in Ref. 4, the PES by Gilibert *et al.* indeed introduces an undesirable artificial potential barrier, however its presence seems to be unimportant at high collision energies. For reference, the cross section of reaction (1) on

the $^4A'$ PES, shown by the dashed black line, is considerably smaller than that on the $^2A'$ PES and has a higher threshold energy of channel opening.

The global rate of NO formation via reaction (1) is compared to the available data in Fig. 4. The present rate coefficient has a good agreement with the similar QCT calculations conducted by Bose and Candler⁴ on older PESs and with experimental measurements by Wray and Teare.²⁰ The largest disagreement with the previous QCT data is observed at temperatures below 2000 K, where the influence of PES peculiarities on the energy transfer is more pronounced. The present results are within the uncertainty interval given by Bortner.²¹ The present QCT simulation augments the conclusion made by Bose and Candler about strong disagreement of results with the rate coefficient by Park,²² which was derived from the backward reaction rate coefficient using the equilibrium constant. It should be noted that in later works by Park *et al.*²³ a more accurate rate constant by Bose and Candler for Eq. (1) was used.

The variation of cross section of reaction (1) with the initial rotational quantum number is shown in Fig. 5 at collisional energies of 0.6 and 1.2 eV on the $^2A'$ PES. As one can see, the present data have intermediate values between the results reported in Refs. 4 and 19. At these conditions, the initial rotational energy of reactants has no significant influence on the cross section of the Zeldovich mechanism, since the collisional energy is significantly larger than the potential barrier. At the low collision energy of 0.6 eV, the present data are closer to the work by Bose and Candler, while at the energy of 1.2 eV, the present cross section is noticeably smaller than the latter.

The vibrationally resolved rate of the Zeldovich reaction is shown in Fig. 6 in the range of trans-rotational temperature between 1000 and 14000 K. The bold lines correspond to the present results for $v_i = 0, 1, 2, 3, 5, 7, 10$ and 15. Symbols correspond to the rates by Bose and Candler. Two red lines describe the contribution of the ground vibrational state from the $^2A'$ and $^4A'$ PESs. The comparison shows a good agreement between two independent simulations for low-lying

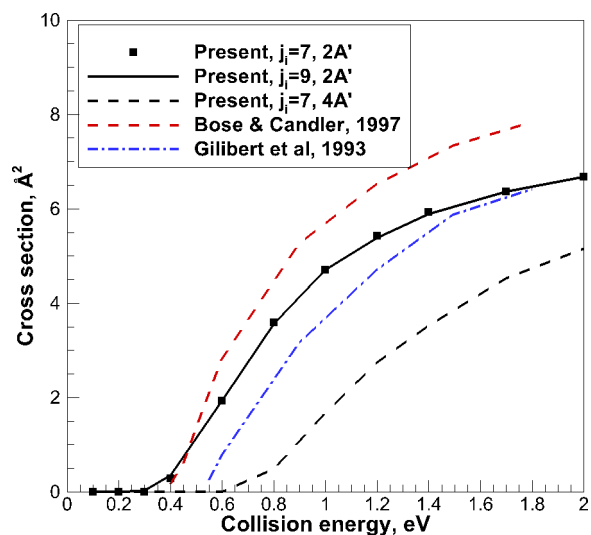


FIG. 3. Integral cross section of transition $O_2(v_i = 0, j_i) + N \rightarrow NO + N$, $j_i = 7$ and 9.

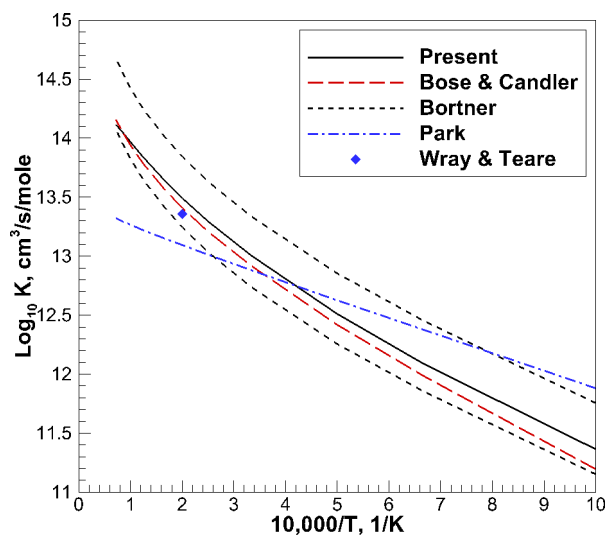


FIG. 4. Thermal equilibrium rate of NO formation.

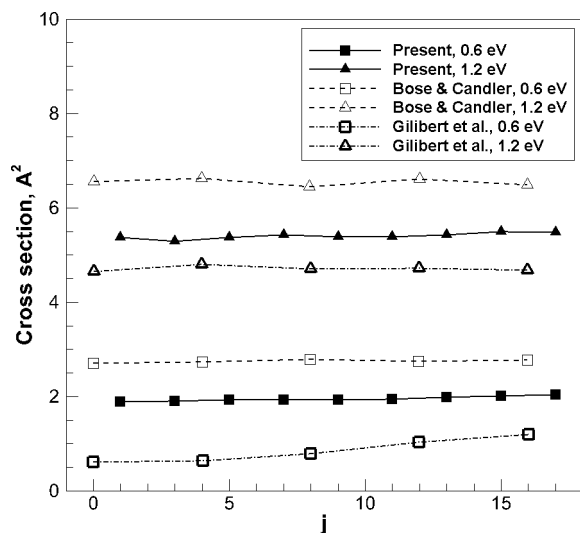


FIG. 5. Variation of cross section of $O_2(v_i=0, j_i)+N \rightarrow NO+N$ reaction, $j_i=1 \dots 17$.

vibrational states at low temperatures and in the entire range of vibrational quanta at high temperatures. However, the rate of Zeldovich mechanism involving vibrationally excited oxygen is underestimated in the calculations by Bose and Candler at temperatures lower than 5000 K. This may be due to some differences in the O_2 vibrational energy ladder. The present vibrational energies are obtained by the Wentzel-Kramers-Brillouin method from the extended-Rydberg two-body potential energy curve.¹² Simulation by Bose and Candler adopts the analytical dependence of energy on vibrational quantum number, leading to a difference of 0.021 eV at $v_i=15$. Yet another reason for this disagreement is the more pronounced influence of topological differences in the attractive part of the PESs at lower collisions energies. One should note an increasing contribution of the $4A'$ PES at temperatures of 4000 K and higher.

Vibrationally resolved rates of O_2 -N non-reactive and exchange collisions are shown in Figs. 7 and 8, respectively.

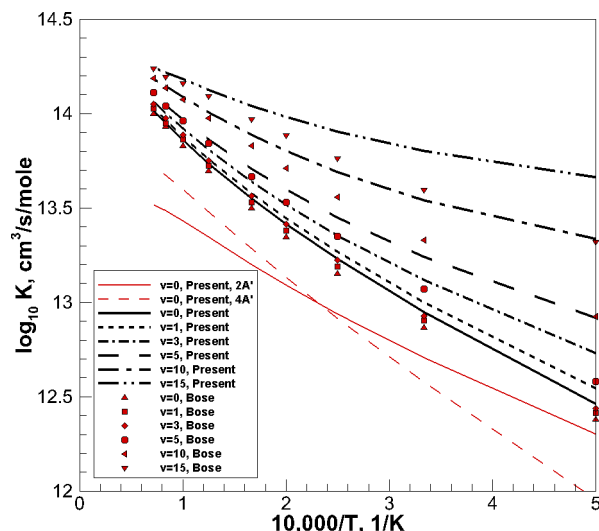


FIG. 6. Variation of $O_2(v_i)+N \rightarrow NO+N$ reaction rate with trans-rotational temperature.

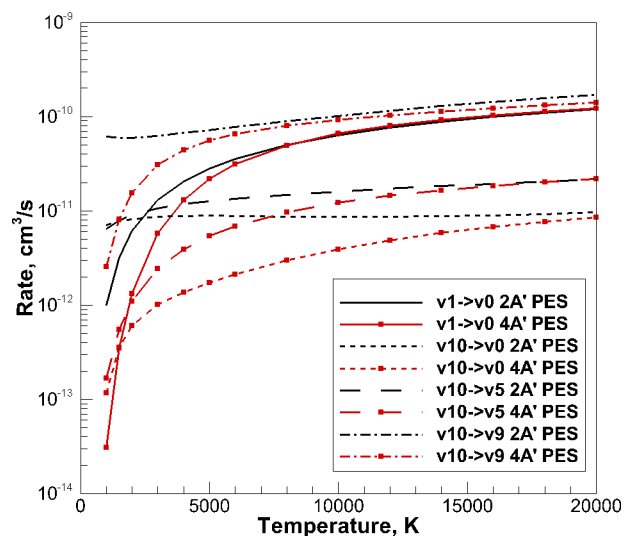


FIG. 7. Rates of $O_2(v_i)+N \rightarrow O_2(v_f)+N$.

In these calculations, the rotational spectrum of rates is averaged at $T_{rot}=T$. The rates of mono- and multi-quantum vibrational deactivation are strongly dependent on the potential energy surface, as follows from Fig. 7. The randomization of vibrational energy via the $2A'$ PES is more efficient than for the $4A'$ PES in the region of low to moderate temperatures. This is especially true for excited vibrational states.

There are also some differences in the final vibrational state of NO between the $2A'$ and $4A'$ surfaces. At translational temperature of 3000 K, the exchange channel is more probable for the $2A'$ PES, as can be judged by the appearance of the solid curves in Fig. 8. However, the rate of production of $NO(v_f=13)$ from $O_2(v_i=10)$ via $4A'$ is higher than $NO(v_f=10)$. At higher temperatures, the situation is opposite: the $4A'$ PES is more efficient in generating excited states of nitric oxide than the $2A'$ PES. The temperature dependences of rates for 10 000 and 16 000 K are similar for both PESs,

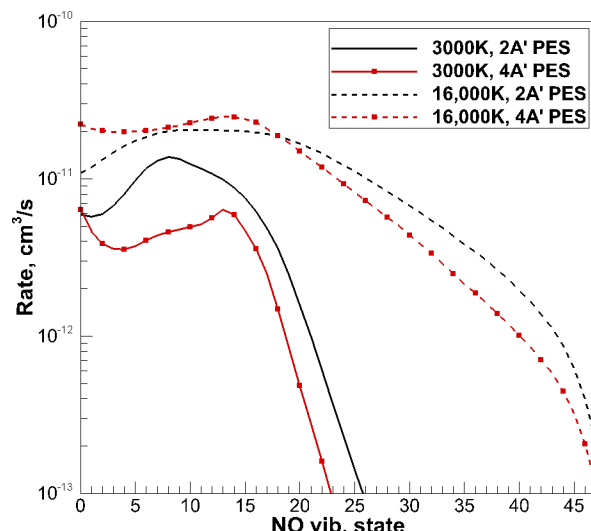


FIG. 8. Rates of $O_2(v_i=10)+N \rightarrow NO(v_f)+O$, at $T=3000, 10000$ and 16000 K.

indicating that the influence of the potential barrier is small at these conditions.

B. Thermalization of O₂ rovibrational ladder

The solution of master equations provides insight into the evolution of the rovibrational manifold during thermalization of oxygen in nonreactive collisions with nitrogen atoms. By analyzing the rovibrational distribution function generated on the ²A' and ⁴A' surfaces, it is possible to judge about the influence of PES topographical features on the process of rovibrational relaxation. In order to simplify the analysis, dissociation and tunneling are artificially excluded from the simulations in this section. The evolution of population of the O₂ rovibrational ladder towards the equilibrium state is presented in Figs. 9-12 for the ²A' and ⁴A' PESs at translational temperatures of 5000 and 10 000 K.

At the early stage of relaxation, the population of the ladder substantially differs from the equilibrium state, shown by the green symbols. When comparing the thermalization process between the two lowest O₂N PESs, it is possible to see that in the case of ²A' the scatter of the populations is noticeably smaller than that in the ⁴A' PES for the same translational temperature. This is explained by higher rates of mono- and multi-quantum transitions, as follows from Fig. 7, and thus, more effective re-distribution of energy between internal states. One of the possible reasons for this is the existence of the NO₂(X) potential well that correlates with the ²A' PES which results in effective “scrambling” of internal states. The tails of distributions are strongly scattered, due to the absence of an exchange channel which appears to be an important mechanism of relaxation for quasi-bound states.⁷ At the late stage of relaxation, the rovibrational manifold becomes depleted into separate strands, each of which corresponds to a particular vibrational state.

Vibrational and rotational relaxation times characterize the rate of thermalization of the rovibrational manifold toward the equilibrium conditions. Using the energy transfer rates, generated in the present work, it is possible to obtain O₂-N

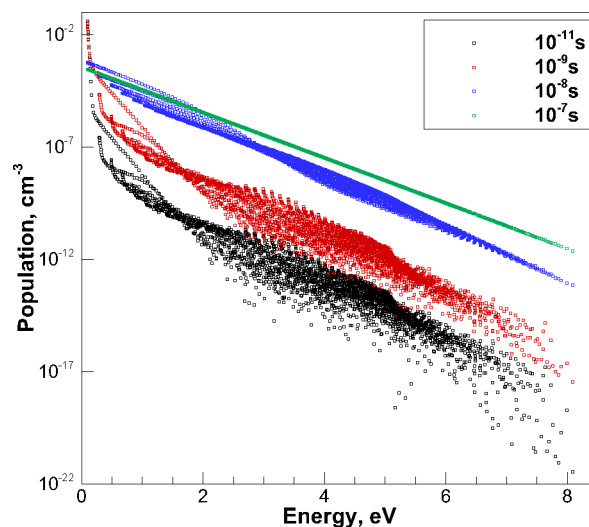


FIG. 10. Population of rovibrational ladder, ⁴A' PES, T = 5000 K.

τ_{vib} and τ_{rot} by solving the system of master equations and taking into account all relevant energy states and transitions, contributing to the relaxation. In this work, such analysis is performed for the ²A' and ⁴A' PESs individually, as well as considering them in a concurrent manner.

First, the situation when $T = T_{rot}$ is considered. The trans-rotational equilibrium is typically observed in hypersonic flows at temperatures less than 8000-10 000 K. This assumption has to be verified for each collisional pair individually, since, as it was shown recently,²⁴ the vibrational and rotational relaxation times for molecular systems with small or zero potential barrier of the enter/exit channel have very similar values.

The populations of $v = 0$ and $v = 1$ account for at least 90% of the entire vibrational ladder for temperatures below 2000 K. Thus, the two-state model provides important insight into the process of vibrational relaxation. The total cross section of monoquantum deactivation from rovibrational level $v_i = 1, j_i$ to $v_f = 0$, and any j_f is obtained by utilizing Eq. (9).

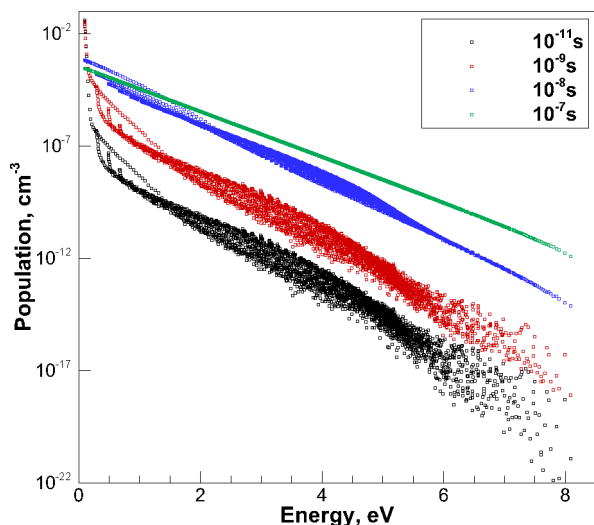


FIG. 9. Population of rovibrational ladder, ²A' PES, T = 5000 K.

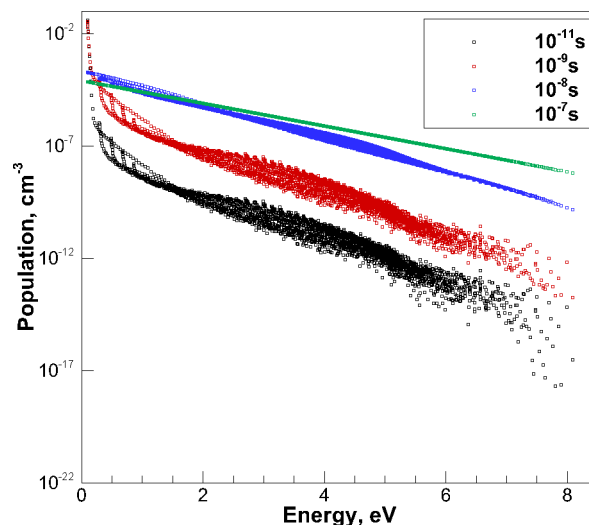
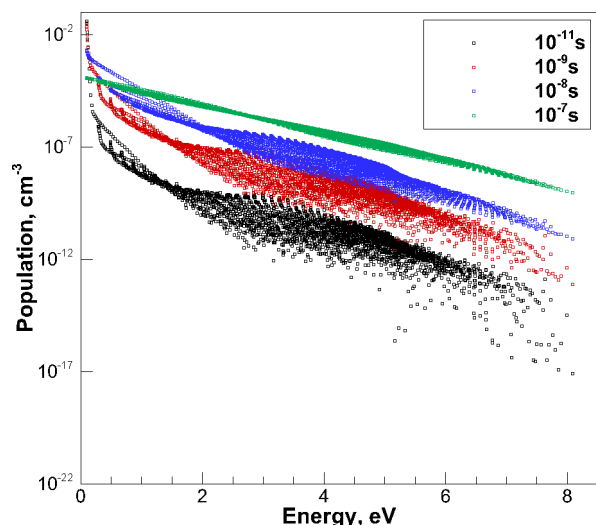


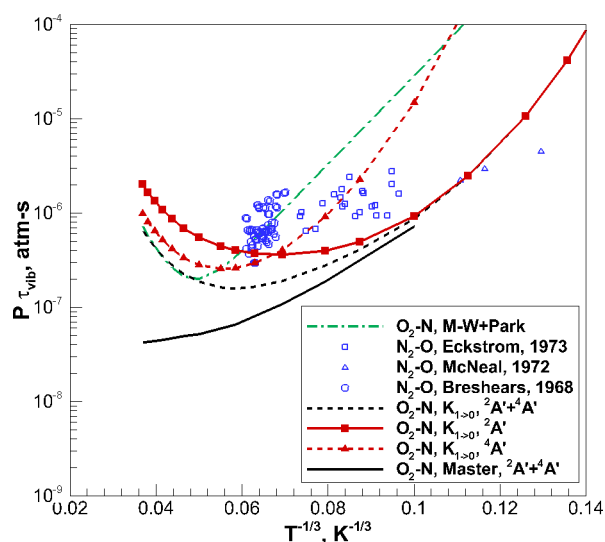
FIG. 11. Population of rovibrational ladder, ²A' PES, T = 10 000 K.

FIG. 12. Population of rovibrational ladder, $4A'$ PES, $T = 10\,000$ K.

The rate of the process $(v_i, j_i) \rightarrow v_f$ is calculated using Eq. (10). The corresponding rate $K_{v_i, j_i \rightarrow v_f}$ is averaged over the initial rotational levels j_i , assuming $T_{rot} = T$, to obtain the rate of monoquantum deactivation $K_{1 \rightarrow 0}$. Then the two-state vibrational relaxation time is obtained as follows:

$$P\tau_{vib} = \frac{k_B T}{K_{1 \rightarrow 0} - K_{0 \rightarrow 1}}, \quad (20)$$

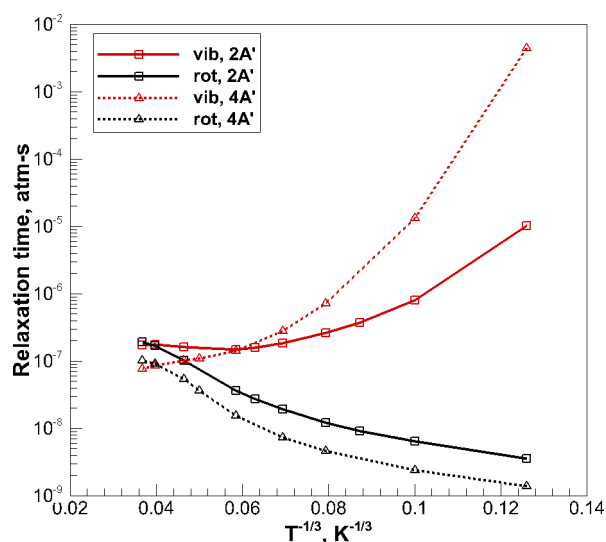
where P is the partial pressure created by projectile particles. At high temperatures, however, Eq. (20) fails to describe the contribution of highly excited vibrational states. The e-folding method by Park²⁵ can be used to obtain τ_{vib} and τ_{rot} , when trans-rotational equilibrium conditions do not hold. The relaxation times, derived from Eq. (20) and from the master equation results including rates from the $2A'$ and $4A'$ PESs, are shown in Fig. 13 with unsymboled dashed and solid lines, respectively. The individual contributions of the $2A'$ and $4A'$ potential energy surfaces in Eq. (20) are shown by lines with square and delta symbols, respectively. The Millikan and

FIG. 13. O_2 -N (VT model) and N_2 -O vibrational relaxation times assuming trans-rotational equilibrium.

White relaxation time, based on the reduced mass of the O_2 -N system and the characteristic vibrational frequency of oxygen, $\omega_e = 1580.193$ cm^{-1} , is shown by the dashed-dotted line. The Park's correction is added to the Millikan-White relaxation time in order to take into account the non-adiabatically of collisions at high temperatures. Finally, the relaxation time in N_2 -O collisions, obtained in Refs. 26–28 and used by Park¹¹ to model the O_2 -N vibrational relaxation, is shown by symbols.

The contribution of the lowest $2A'$ PES on vibrational relaxation dominates at kinetic temperatures below 3000 K. At higher temperatures, the first excited PES governs the vibrational relaxation, while the contribution of the ground PES becomes small, but non-vanishing. A deviation of the relaxation time, derived by Eq. (20), from the e-folding relaxation time is observed for temperatures as low as 2000 K. This can be attributed to the influence of excited vibrational states and multiquantum transitions. The present data for the O_2 -N system show satisfactory agreement with the N_2 -O relaxation time only at low temperatures, while at high temperature the calculated O_2 -N relaxation time is nearly an order of magnitude lower than that in N_2 -O collisions. The Millikan-White equation strongly overestimates the vibrational relaxation time, showing an inadequacy of its utilization for collisions that involve multiple PESs with a deep minimum of potential energy. At high temperatures, the Millikan-White time, owing to the Park's correction, indicates surprisingly good agreement with the relaxation time derived from Eq. (20). However, the influence of multi-quantum processes and vibrational states with $v > 1$ is quite significant at these temperatures, making the overall vibrational relaxation time, derived from the solution of master equations, substantially lower. Besides the influence of multi-quantum jumps and relaxation to/from excited states, there are other factors resulting in the failure of the Millikan-White correlation, such as exchange and dissociation channels, and the anharmonicity of vibrational ladder.

Figure 14 presents the O_2 -N vibrational and rotational relaxation times obtained by means of the e-folding method

FIG. 14. O_2 -N vibrational and rotational relaxation times, RVT thermodynamic model.

and the RVT thermodynamic model. The intermolecular attraction and the lower potential barrier of the $^2A'$ PES results in much faster vibrational relaxation, compared to the $^4A'$ PES at low temperatures. Above 5000 K, the vibrational relaxation via the $^4A'$ PES becomes more efficient than via the $^2A'$ PES. The assumption about rotational equilibrium in O_2 -N collisions is valid for temperatures below 8000 K. Above this point, the vibrational and rotational modes should be treated in a concurrent manner. At very high temperatures (above 16 000 K), τ_{rot} exceeds τ_{vib} for both PESs. A possible explanation of this fact lies in the absence of the exchange channel in the O_2 -N system. A similar behavior of relaxation times is observed for N_2 -N,⁷ when the exchange channel is artificially excluded from the master equation simulation. The exchange channel is an efficient mechanism for scrambling of internal states, and, due to non-symmetry of the O_2 -N system, such mechanism of thermalization is not available.

A comparison of O_2 vibrational and rotational relaxation times in collisions with different projectiles, obtained via the QCT method and master equation simulation, is shown in Fig. 15. Square symbols correspond to O_2 -N, triangular and circular symbols describe the data on O_2 -O²⁹ and O_2 -Ar,³⁰ respectively. In the range of moderate to low temperatures, the fastest relaxation time is observed in the O_2 -O system. This is due to the absence of a potential barrier in the entrance/exit channel of the ozone complex.³¹ The energy randomization between target and projectile in the O_3 complex is very efficient, particularly due to the large contribution of the exchange channel. This results in the decrease of relaxation time with temperature, since the probability of vibrational transition is smaller for highly energetic collisions.

On the contrary, a system with a strongly repulsive potential, such as O_2 -Ar, demonstrates the typical Millikan-White behavior of the relaxation time, which can be fit by a linear dependence in the $P\tau$ - $T^{-1/3}$ coordinates. At high kinetic temperatures, the principles of Landau-Teller theory break down, which leads to the deviation of the relaxation time from

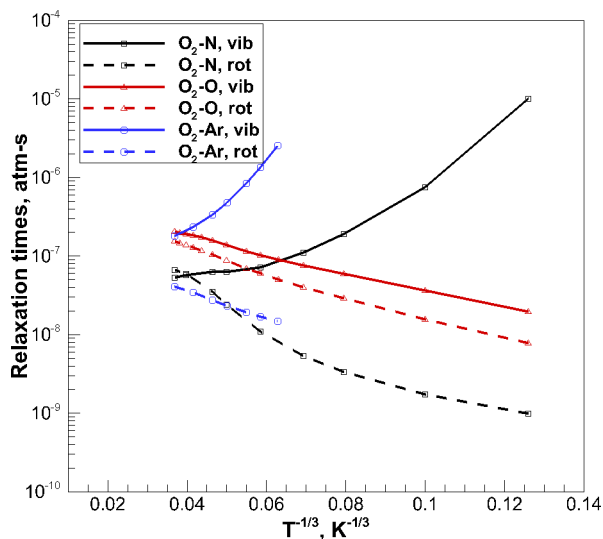


FIG. 15. Comparison of O_2 -N, O_2 -Ar and O_2 -O relaxation times.

TABLE I. O_2 -N master equation vibrational and rotational relaxation times, [atm-s], RVT and VT models.

Temperature	Vibrational (RVT)	Rotational (RVT)	Vibrational (VT)
500.0	1.007×10^{-5}	9.896×10^{-10}	1.008×10^{-5}
1000.0	7.479×10^{-7}	1.732×10^{-9}	7.206×10^{-7}
2000.0	1.906×10^{-7}	3.339×10^{-9}	1.862×10^{-7}
3000.0	1.103×10^{-7}	5.329×10^{-9}	1.083×10^{-7}
5000.0	7.176×10^{-8}	1.090×10^{-8}	6.573×10^{-8}
8000.0	6.326×10^{-8}	2.416×10^{-8}	5.164×10^{-8}
10000.0	6.235×10^{-8}	3.519×10^{-8}	4.933×10^{-8}
16000.0	5.729×10^{-8}	5.930×10^{-8}	4.365×10^{-8}
20000.0	5.301×10^{-8}	6.695×10^{-8}	4.202×10^{-8}

the linear dependence. The temperature dependence of the vibrational relaxation time in O_2 -N collisions demonstrates the behavior of a molecular system with a large repulsive component in the PES, which becomes important at high energies. At low temperatures, the O_2 -N relaxation time is several orders of magnitude lower than that in the purely repulsive molecular system, which confirms the importance of the PES that has low potential barrier and correlates with $NO_2(X^2A_1)$ for the process of vibrational relaxation.

The relaxation times, obtained from the solution of master equations using the RVT and VT thermodynamic models, are given in Table I. A combination of two exponential functions can be used to generate curve fit parameters that can be used in fluid dynamic codes,

$$P\tau = \exp(a(T^{-1/3} - b)) + \exp(c(T^{-1/3} - d)), \quad (21)$$

where $P\tau$ is in atm-s, translational temperature T is in K, coefficients a, b, c , and d are given in Table II.

C. Thermal relaxation in the presence of dissociation

The system of master equations, coupled to the set of bound-bound and bound-free transition rates, provides a convenient tool for the study of coupled relaxation-dissociation mechanisms in the heat bath of nitrogen atoms. Following this approach, it is possible to study the validity of the quasi-state state (QSS) assumption for two different PESs and derive the QSS dissociation rate coefficient and the average loss of internal energy during the phase of active chemical transformations.

The variation of O_2 vibrational and rotational temperatures is shown in Figs. 16 and 17 for the $^2A'$ and $^4A'$ PESs, respectively. In these simulations, the total number density of particles is set to 10^{18} cm^{-3} with 5% molar

TABLE II. Curve fit parameters of vibrational and rotational relaxation times, given in Table I.

Mode	a	b	c	d
Vibrational (RVT model)	101.6	0.2397	12.72	1.3561
Rotational (RVT model)	-16.51	-1.1296	-96.56	-0.1338
Vibrational (VT model)	-4.291	-3.9641	71.91	0.2972

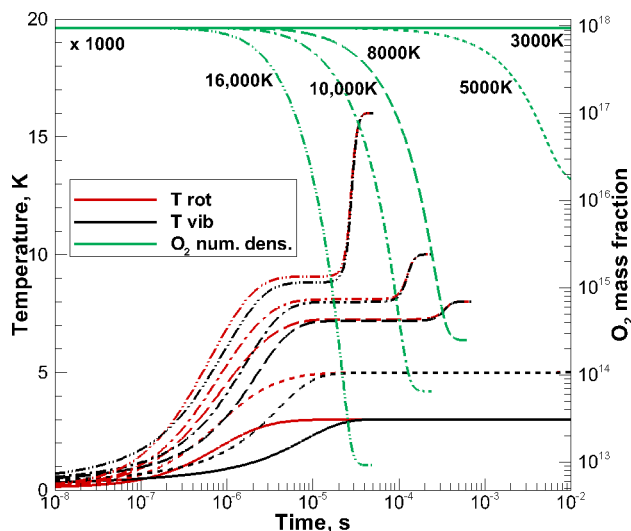


FIG. 16. T_{vib} , T_{rot} , and O_2 number density in the presence of dissociation/recombination reactions, $^2A'$ PES.

fraction of nitrogen atoms. No atomic oxygen is introduced initially. The RVT thermodynamic model is considered. For temperatures below 8000 K, thermal relaxation occurs prior to the onset of dissociation. At these conditions, the O_2 depletion does not take place immediately after the rotational mode is thermalized, but when the vibrational equilibrium occurs. This means that the dissociation preferentially occurs from higher vibrational levels at low temperatures. With the translational temperature increasing further, the quasi-steady internal temperatures deviate from the equilibrium level, since the rates of dissociation and thermal relaxation become comparable. Only a small amount of atomic oxygen is generated prior to the QSS phase at temperatures of 8000 and 10 000 K, indicating the validity of the QSS assumption at these conditions. However, at $T = 16\,000$ K, nearly half of the oxygen molecules have already dissociated prior to the QSS phase, which means the breakdown of the QSS approach. This conclusion can be made for both PESs.

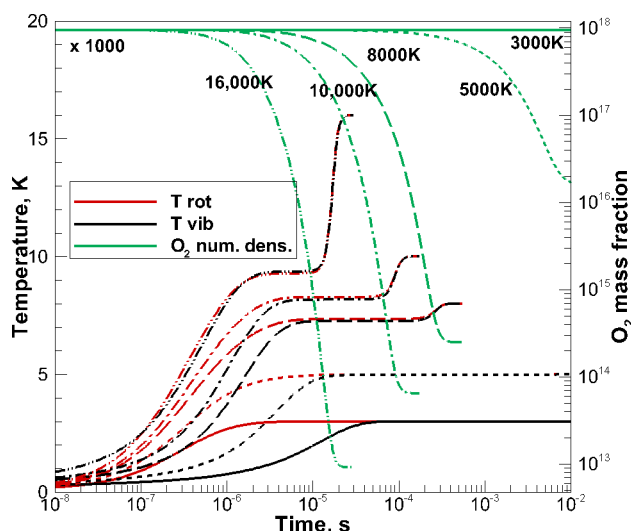


FIG. 17. T_{vib} , T_{rot} , and O_2 number density in the presence of dissociation/recombination reactions, $^4A'$ PES.

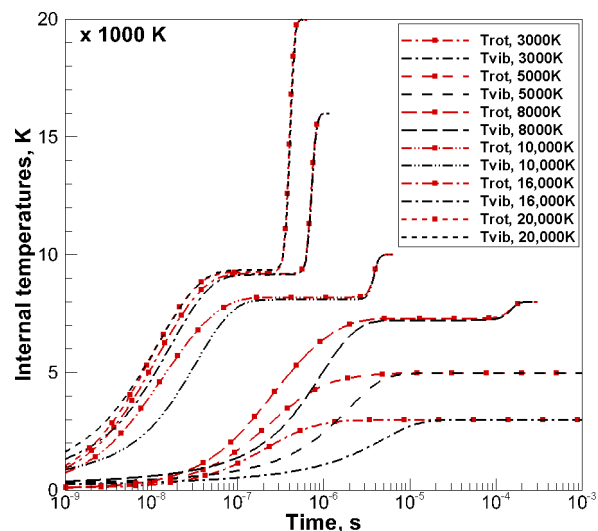


FIG. 18. Rovibrational thermalization via $^2A'$ and $^4A'$ PESs simultaneously.

The rovibrational thermalization via concurrent relaxation on the $^2A'$ and $^4A'$ PESs is shown in Fig. 18. The quasi-steady vibrational and rotational temperatures monotonically increase at low T , eventually reaching a constant level. This level is just below the value of 10 000 K. At high temperatures, the vibrational and rotational temperatures closely follow each other. In this case, reduced order modeling of O_2 -N thermalization can be performed using a unified internal temperature that describes the distribution of both vibrational and rotational degrees of freedom. The information about T_{vib} during the QSS phase can be used for verification of dissociation rates in the presence of vibrational nonequilibrium, proposed in the literature.^{32,33}

The utilization of a state-resolved approach to model nonequilibrium hypersonic flows can be computationally impractical in everyday practice. In order to describe the coupling between the processes of rovibrational relaxation and dissociation, it is convenient to define the energy rate constants that describe the average loss of internal energy in a single dissociation event. This step is important for the development of reduced order models of aerothermochemistry. The coupling coefficient, $C_{x,i}$, where x denotes the vibrational, rotational, or rovibrational mode, can be defined for each internal state as well as for the entire vibrational or rotational manifold. The state-specific coupling coefficient is estimated as follows:

$$C_{x,i} = \frac{D_i n_{O_2} n_i^{eq} (\rho_O^2 - \rho_i) e_{x,i}}{\sum_i D_i n_{O_2} n_i^{eq} (\rho_O^2 - \rho_i)}, \quad (22)$$

where ρ denotes the number density of species normalized with respect to its own equilibrium value, $e_{x,i}$ stands for the corresponding internal energy, and D_i is the state-specific dissociation rate coefficient. Summation of $C_{x,i}$ over the entire rovibrational ladder produces the average coupling coefficient C_x that can be utilized in the formulation of a vibrational energy equation in multi-temperature models.³⁴ In the present work, the energy rate coefficients, given by Eq. (22), are normalized by the classical dissociation energy D_e of oxygen.

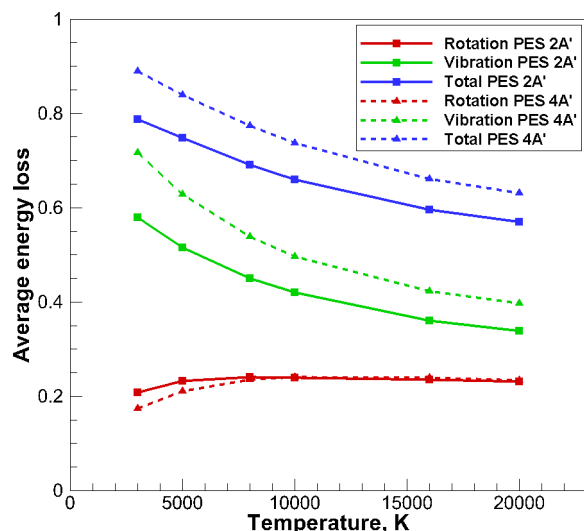


FIG. 19. Energy loss coefficients due to dissociation, $\text{O}_2\text{-N}$ collisions, $^2\text{A}'$ and $^4\text{A}'$ PESs.

The average loss of internal, vibrational, and rotational energies is shown in Fig. 19 for the $^2\text{A}'$ and $^4\text{A}'$ PESs by curves with square and triangular symbols. The differences in the PES topology weakly influence the removal of rotational energy in the range of temperatures between 3000 and 20000 K. The influence of the particular PES on the loss of vibrational energy is more pronounced. The low-lying $^2\text{A}'$ potential energy surface with the lower barrier and deeper potential minimum suggests smaller loss of vibrational, and, consequently, the internal energy, compared to that in the $^4\text{A}'$ PES in the entire temperature range. The difference in C_{vib} is largest at $T = 3000$ K, i.e., at conditions when the influence of the potential barrier is significant.

An overview of available C_{rot} and C_{vib} for molecular oxygen in collisions with different projectiles is given in Fig. 20. The $\text{O}_2\text{-N}$, $\text{O}_2\text{-Ar}$, and $\text{O}_2\text{-O}$ systems are shown with solid, dashed, and dashed-dotted lines, respectively. The $\text{O}_2\text{-O}$

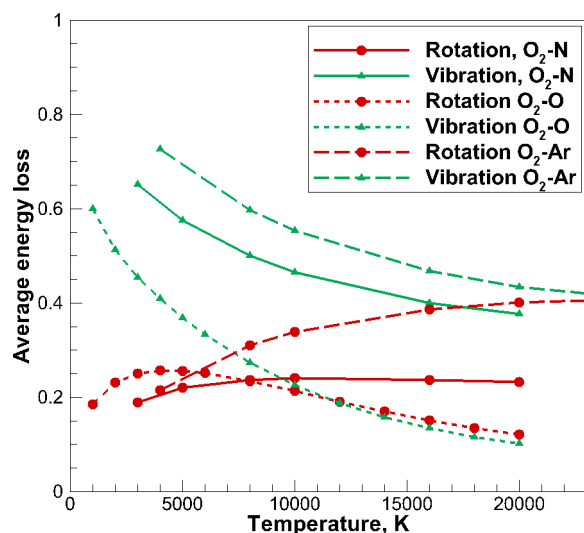


FIG. 20. Energy loss coefficients due to dissociation, $\text{O}_2\text{-X}$ collisions, where X is N, Ar, and O.

data¹⁸ represent the energy loss coefficients in the presence of a strongly attractive, barrierless potential.³⁵ On the contrary, the $\text{O}_2\text{-Ar}$ data³⁰ are obtained assuming a purely repulsive Buckingham potential.³⁶ The $\text{O}_2\text{-N}$ energy loss coefficients are obtained by concurrent master equation simulations using rates from the $^2\text{A}'$ and $^4\text{A}'$ PESs and their statistical weights.

Among the considered projectiles, the $\text{O}_2\text{-O}$ interaction has the smallest coupling coefficient C_{vib} and the most rapid decrease of C_{vib} with temperature. As discussed previously,¹⁸ this is the effect of the barrierless potential energy surface. The dissociation rate coefficient in $\text{O}_2\text{-O}$ collisions rapidly increases with translational temperature, while the vibrational relaxation time has a weak temperature dependence. This results in the incomplete thermalization before the onset of dissociation at high temperatures. The vibration-dissociation coupling coefficient for the $\text{O}_2\text{-N}$ system is smaller than that in $\text{O}_2\text{-Ar}$ collisions and has a similar temperature dependence.

The temperature dependence of C_{rot} for $\text{O}_2\text{-O}$ and $\text{O}_2\text{-N}$ significantly differs from that in $\text{O}_2\text{-Ar}$. The latter rapidly increases with temperature, approaching C_{vib} . This is explained by a large contribution of rotational states with high energies (in particular, quasi-bound states) in the process of dissociation. On the contrary, the $\text{O}_2\text{-O}$ and $\text{O}_2\text{-N}$ systems have a relatively small C_{rot} , indicating a limited influence of highly excited rotational states. The state-specific and cumulative $\text{O}_2\text{-N}$ C_{vib} and C_{rot} are shown in Figs. 21 and 22 for a temperature of 10000 K. Cumulative coefficients are normalized to their own maximum value. While the relative contribution of states into the integral value of the energy rate coefficient is nearly the same for both the $^2\text{A}'$ and $^4\text{A}'$ PESs, the absolute contribution of quasi-bound states into C_{rot} and C_{vib} is higher for the $^4\text{A}'$ PES. In other words, pre-dissociated states have a more pronounced influence on the dissociation process in the case of repulsive atom-molecule interaction. A similar conclusion about the importance of QB states is drawn in Ref. 7 for the $\text{N}_2\text{-N}$ system.

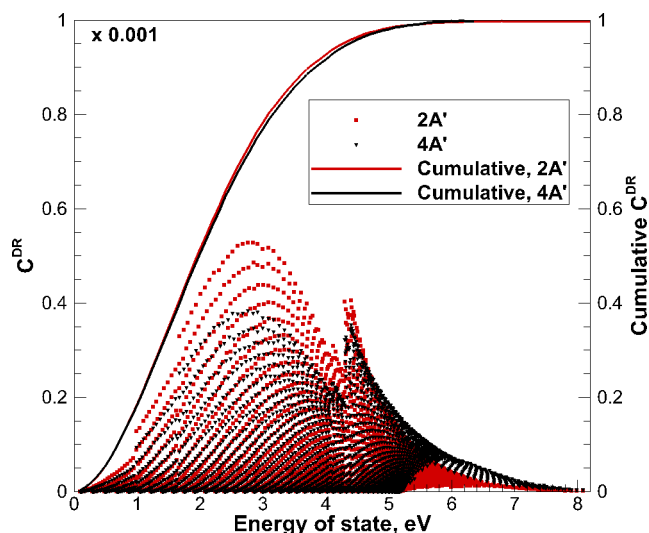


FIG. 21. Quasi-stationary state-specific energy loss coefficients, rotational mode, $T = 10000$ K.

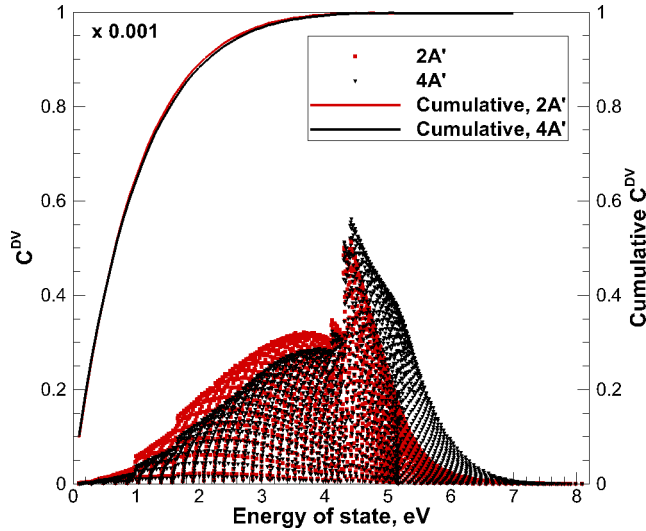


FIG. 22. Quasi-stationary state-specific energy loss coefficients, vibrational mode, $T = 10\,000$ K.

Dissociation rate coefficients, obtained via the master equation simulations on the $^2A'$ and $^4A'$ PESs, are shown in Fig. 23. Red line and square symbols correspond to the dissociation rate coefficient, estimated during the QSS phase on the $^2A'$ PES and $^4A'$ PES separately. Circular symbols correspond to the QSS dissociation rate coefficient obtained by taken into account contributions via $^2A' + ^4A'$ PESs and $^6A'$ PES using Eq. (5). Similarly, the black line, triangular symbols and blue line correspond to the thermal equilibrium dissociation rate, estimated from state-specific QCT data assuming $T = T_{vib} = T_{rot}$. The long dashed line corresponds to the dissociation rate proposed by Park³⁷ and evaluated using the governing temperature $T_a = \sqrt{TT_{vib}}$, where T_{vib} corresponds to vibrational temperature during the QSS phase in Fig. 18. These parameters are shown in Table III. The columns D_{eq} and D_{QSS} describe the dissociation rate coefficients at thermal equilibrium and during QSS phase

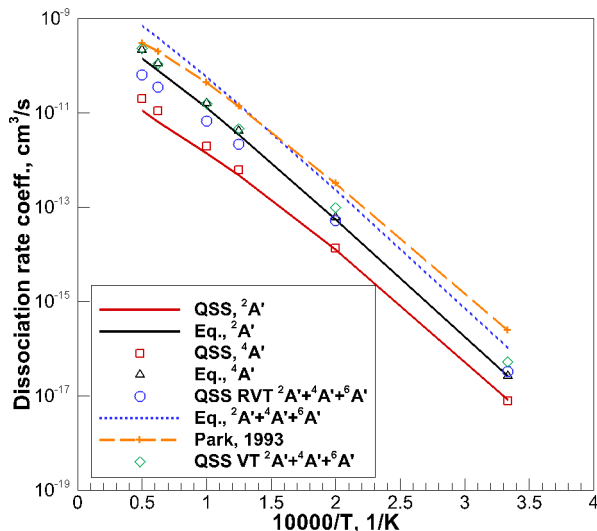


FIG. 23. O_2 -N quasi-stationary and thermal equilibrium dissociation rate coefficients.

TABLE III. Total O_2 -N thermal equilibrium and quasi-stationary dissociation rates coefficients obtained on $^2A' + ^4A'$ PESs. Contribution of $^6A'$ PES is taken into account by doubling the dissociation rate coefficient on the two lowest PESs.

T	T_{vib} , QSS	D_{eq}	$D_{Park}(\sqrt{TT_{vib}})$	D_{QSS}
3 000	3000.0	1.043×10^{-16}	2.461×10^{-16}	3.272×10^{-17}
5 000	4965.2	2.300×10^{-13}	3.085×10^{-13}	5.188×10^{-14}
8 000	7215.7	1.504×10^{-11}	1.002×10^{-11}	2.166×10^{-12}
10 000	8090.6	5.696×10^{-11}	2.541×10^{-11}	6.664×10^{-12}
16 000	9152.5	3.818×10^{-10}	8.531×10^{-11}	3.484×10^{-11}
20 000	9442.9	7.052×10^{-10}	1.240×10^{-10}	6.252×10^{-11}

obtained from the concurrent solutions of the master equations on the $^2A'$, $^4A'$ PESs and adding the contribution of $^6A'$ PES via Eq. (5).

Both QSS and thermal equilibrium dissociation rate coefficients are nearly identical for the two lowest O_2N PESs. The quasi-steady state dissociation rate coefficient is lower than the equilibrium dissociation rate due to the incomplete thermalization of the rovibrational degrees of freedom. For the entire range of considered temperatures, Park's rate substantially overestimates the present D_{QSS} by a factor of 2–7.5. The QSS and thermal equilibrium dissociation rate coefficients are curve fitted to the standard Arrhenius form. The corresponding parameters are given in Table IV.

D. Validity of multi-temperature model

This section investigates the accuracy of the multi-temperature (MT) model for the description of O_2 dissociation in the presence of vibrational nonequilibrium. The QCT simulations provide new high-fidelity data, such as the thermal equilibrium dissociation rate and the average loss of energy due to depletion, that can be incorporated into the MT model. To simplify the analysis, only vibrational nonequilibrium is modeled. The results of the MT model are compared with those by state-resolved master equation simulations coupled to the set of $^2A' + ^4A'$ PES rates of the bound-bound and bound-free transitions. The governing equations of the zero-dimensional MT model are as follows:

$$\frac{\partial(\rho e_v)}{\partial t} = \rho_{O_2} \frac{e_v^* - e_v}{\tau_{vib}} + \dot{\omega}_{O_2} C^{Dv} D_e, \quad (23)$$

$$\dot{\omega}_{O_2} = R(T_a) n_O^2 n_N - D(T_a) n_{O_2} n_N.$$

In Eq. (23), e_v and e_v^* are the O_2 vibrational energy evaluated at T_{vib} and T , respectively, ρ and ρ_{O_2} are the density

TABLE IV. O_2 -N Arrhenius coefficients of dissociation process. Contribution of $^6A'$ PES is taken into account by doubling the rate coefficient on two lowest PESs.

Rate coefficient	$\log(A)$, cm^3/s	B	C, K
QSS RVT	-8.254	-1.2480	59 020
QSS VT	-14.310	-0.5159	56 940
Equilibrium	-10.410	-0.7720	60 620

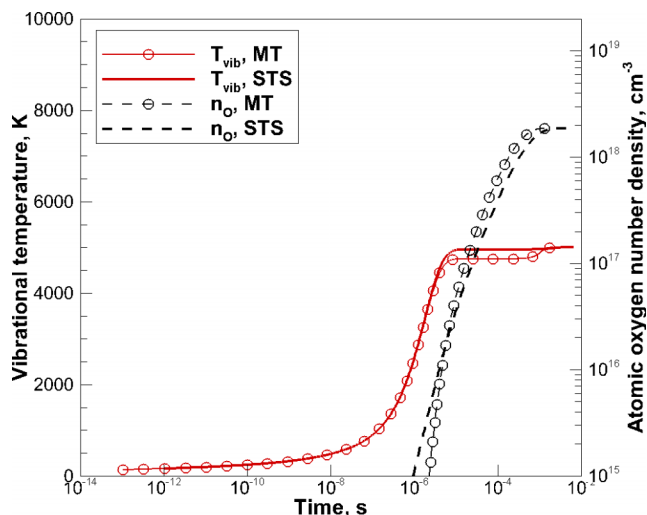


FIG. 24. Vibrational temperature and n_{O} at $T = 5000$ K, present thermal equilibrium dissociation rate coefficient and Park model.

of $\text{O}_2\text{-O}$ mixture and partial density of O_2 , D_e is the classical dissociation energy, τ_{vib} is the $\text{O}_2\text{-N}$ relaxation time, taken from Fig. 13, solid black line. The only type of collision considered is between O_2 and N. Initially, the total number density is set to 10^{18} cm^{-3} with 5% of atomic nitrogen molar fraction. The vibration-dissociation coupling is via Park's model.³⁷ The governing temperature T_a is calculated as $\sqrt{TT_{\text{vib}}}$. The global recombination rate coefficient, R , is estimated from D via the principle of detailed balance. Vibrational energy coupling coefficient corresponds to the loss of internal energy in $\text{O}_2\text{-O}$ collisions in the presence of rotational equilibrium.

The thermal equilibrium dissociation rate coefficient, D_{eq} , is taken from Table III. For the purpose of comparison, instead of Park's model, the actual $\text{O}_2\text{-N}$ QSS dissociation rate coefficient, given in Table III in the last column, is used. When the quasi-steady rate coefficient is utilized, Park's model should not be introduced in Eq. (23). The vibrational temperature and the atomic oxygen number density are

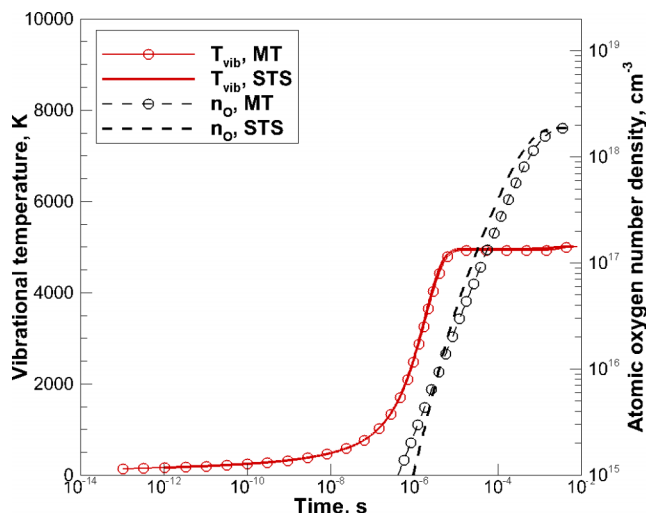


FIG. 25. Vibrational temperature and n_{O} at $T = 5000$ K, QSS dissociation rate coefficient, no Park model.

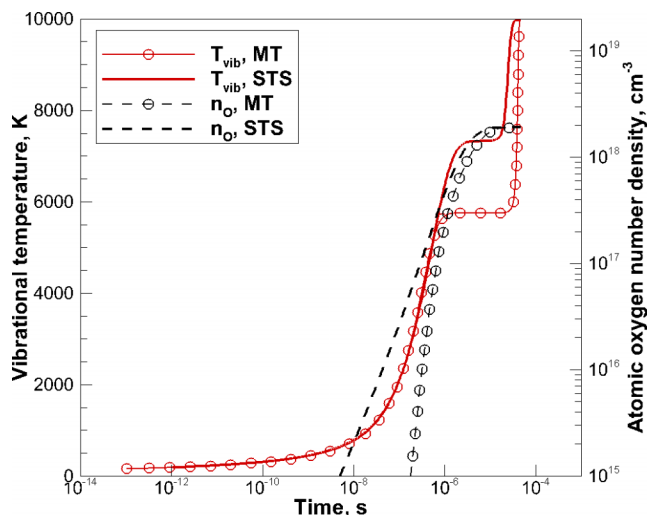


FIG. 26. Vibrational temperature and n_{O} at $T = 10000$ K, present thermal equilibrium dissociation rate coefficient and Park model.

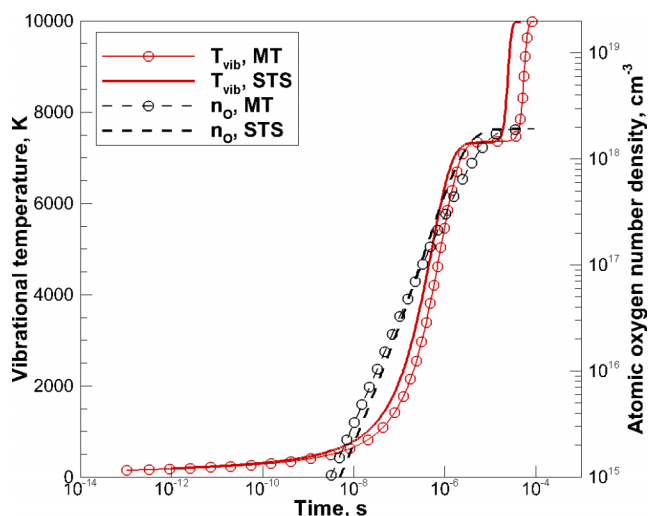


FIG. 27. Vibrational temperature and n_{O} at $T = 10000$ K, QSS dissociation rate coefficient, no Park model.

shown in Figs. 24-27 at heat bath conditions of 5000 and 10000 K. The general observation is that the utilization of the present QSS rate without vibrational-dissociation coupling provides results that are much closer to the master equation solution, compared to Park model. The difference between the latter and the master equation solution is larger when nonequilibrium effects are more pronounced, i.e., at $T = 10000$ K. Since the rate by Park overestimates the actual dissociation rate, the QSS vibrational temperature, given by the MT model, is lower than that by the master equation approach.

IV. CONCLUSION

A comprehensive investigation of $\text{O}_2\text{-N}$ collisional dynamics is conducted using the two lowest $^2\text{A}'$ and $^4\text{A}'$

ab initio potential energy surfaces. In contrast with previous works in this field, the present study is dedicated to the analysis of rovibrational relaxation and dissociation of molecular oxygen. It is found that the O₂-N vibrational relaxation time, obtained from the solution of master equations, is noticeably lower than that in N₂-O collisions, previously assumed as a substitute for the O₂-N molecular system.

The ²A' potential energy surface has a lower potential barrier and demonstrates strong attractive properties, and this results in a significantly faster vibrational relaxation at low temperatures, compared to the ⁴A' PES. The thermalization of the rotational mode is studied as well. Both the ²A' and ⁴A' PESs produce similar rotational relaxation times in the wide range of temperatures observed in hypersonic flows. The solution of master equations indicates the presence of rotational nonequilibrium in O₂-N collisions at temperatures above 8000 K. This fact should be considered when simulating shock flows during re-entry of spacecraft or cruise flight of hypersonic vehicles. At high temperatures, the rotational relaxation becomes faster than the vibrational relaxation. A possible explanation of this phenomenon is that the O₂-N exchange channel leads to products other than initial species, and, thus, does not contribute in the O₂ relaxation mechanism.

Quasi-steady and thermal equilibrium dissociation rate coefficients are reported in the temperature interval between 3000 and 20 000 K. It is shown that the O₂ depletion proceeds with a similar rate coefficient on the ²A' and ⁴A' PESs. The QSS dissociation rate coefficient is found to be lower than the previously assumed data by a factor between 4 and 15. Arrhenius parameters for the new QSS dissociation rate are proposed using Park's multi-temperature model and the values of quasi-steady state vibrational temperature obtained from the solution of master equations. Since the validity of the QSS assumption is questionable at translational temperatures higher than 10 000 K, one should use these curve-fitted data with caution. For temperatures below 10 000 K it is shown that the simple utilization of the QSS dissociation rate coefficient is more accurate than using previously reported rates and models of vibration-dissociation coupling.

Finally, the relaxation-dissociation coupling coefficients that describe the loss of internal energy due to dissociation are derived. The present O₂-N vibrational energy rate coefficients takes an intermediate value between those for the O₂-Ar and O₂-O systems. The O₂-N rotational energy rate coefficient exhibits a behavior similar to O₂-O. The absolute value of C_{rot} in O₂-N collisions is substantially lower than in O₂-Ar collisions. For this reason, it is possible to speak about the relative unimportance of highly excited rotational and quasi-bound states in the process of dissociation.

ACKNOWLEDGMENTS

The authors gratefully acknowledge funding for this work through Air Force Office of Scientific Research Grant No. FA9550-12-1-0483.

- ¹Y. Zeldovich, D. Frank-Kamenetskii, and P. Sadovnikov, *Oxidation of Nitrogen in Combustion* (Publishing House of the Academy of Sciences of USSR, 1947).
- ²M. E. Whitson, L. A. Darnton, and R. J. McNeal, *Chem. Phys. Lett.* **41**, 552 (1976).
- ³A. Rahbee and J. Gibson, *J. Chem. Phys.* **74**, 5143 (1981).
- ⁴D. Bose and G. V. Candler, *J. Chem. Phys.* **107**, 6136 (1997).
- ⁵R. L. Jaffe, M. D. Pattengill, and D. W. Schwenke, *Supercomputer Algorithms for Reactivity, Dynamics and Kinetics of Small Molecules* (Springer, 1989), pp. 367–382.
- ⁶J. Livesey, A. Roberts, and A. Williams, *Combust. Sci. Technol.* **4**, 9 (1971).
- ⁷M. Panesi, R. L. Jaffe, D. W. Schwenke, and T. E. Magin, *J. Chem. Phys.* **138**, 044312 (2013).
- ⁸J. G. Kim and I. D. Boyd, *Chem. Phys.* **415**, 237 (2013).
- ⁹I. Armenise and F. Esposito, *Chem. Phys.* **446**, 30 (2015).
- ¹⁰J. D. Bender, P. Valentini, I. Nompelis, Y. Paukku, Z. Varga, D. G. Truhlar, T. Schwartzentruber, and G. V. Candler, *J. Chem. Phys.* **143**, 054304 (2015).
- ¹¹C. Park, *J. Thermophys. Heat Transfer* **20**, 689 (2006).
- ¹²R. Sayós, C. Oliva, and M. González, *J. Chem. Phys.* **117**, 670 (2002).
- ¹³S. P. Walch and R. L. Jaffe, *J. Chem. Phys.* **86**, 6946 (1987).
- ¹⁴G. Herzberg, *Molecular Spectra and Molecular Structure* (van Nostrand, 1957).
- ¹⁵M. H. Alexander and P. J. Dagdigan, *J. Chem. Phys.* **79**, 302 (1983).
- ¹⁶D. G. Truhlar and J. T. Muckerman, *Atom-Molecule Collision Theory* (Springer, 1979), pp. 505–566.
- ¹⁷P. G. Kuntz, in *Atom-Molecule Collision Theory* (Springer, 1979), pp. 669–692.
- ¹⁸D. A. Andrienko and I. D. Boyd, *Phys. Fluids* **27**, 116101 (2015).
- ¹⁹M. Giliert, A. Aguilar, M. González, and R. Sayós, *Chem. Phys.* **172**, 99 (1993).
- ²⁰K. L. Wray, *J. Chem. Phys.* **36**, 2597 (1962).
- ²¹M. Bortner, "A review of rate constants of selected reactions of interest in re-entry flow fields in the atmosphere," Technical Report No. 484, DTIC Document, 1969.
- ²²C. Park, J. T. Howe, R. L. Jaffe, and G. V. Candler, *J. Thermophys. Heat Transfer* **8**, 9 (1994).
- ²³C. Park, R. L. Jaffe, and H. Partridge, *J. Thermophys. Heat Transfer* **15**, 76 (2001).
- ²⁴D. A. Andrienko and I. D. Boyd, "Master equation study of vibrational and rotational relaxations of oxygen," *J. Thermophys. Heat Transfer* (published online).
- ²⁵C. Park, *J. Thermophys. Heat Transfer* **18**, 527 (2004).
- ²⁶D. Eckstrom, *J. Chem. Phys.* **59**, 2787 (1973).
- ²⁷R. J. McNeal, M. E. Whitson, and G. R. Cook, *J. Geophys. Res.* **79**, 1527, doi:10.1029/JA079i010p01527 (1974).
- ²⁸W. Breshears and P. Bird, *J. Chem. Phys.* **48**, 4768 (1968).
- ²⁹D. A. Andrienko and I. D. Boyd, AIAA Paper 2016-0736, 2016.
- ³⁰J. G. Kim and I. D. Boyd, AIAA Paper 2014-2963, 2014.
- ³¹M. Quack and J. Troe, *Ber. Bunsen-Ges. Phys. Chem.* **79**, 170 (1975).
- ³²C. Park, *Nonequilibrium Hypersonic Aerothermodynamics* (Wiley, 1989).
- ³³P. V. Marrone and C. E. Treanor, *Phys. Fluids* **6**, 1215 (1963).
- ³⁴P. A. Gnoffo, R. N. Gupta, and J. L. Shinn, "Conservation equations and physical models for hypersonic air flows in thermal and chemical nonequilibrium," Technical Report, NASA Technical Paper 2867 (National Aeronautics and Space Administration, Office of Management, Scientific, and Technical Information Division, Washington, DC, USA, 1989).
- ³⁵A. Varandas and A. Pais, *Mol. Phys.* **65**, 843 (1988).
- ³⁶A. Gross and G. D. Billing, *Chem. Phys.* **187**, 329 (1994).
- ³⁷C. Park, *J. Thermophys. Heat Transfer* **7**, 385 (1993).